

The light stop window

Antonio Delgado^a, Gian F. Giudice^b, Gino Isidori^{b,c},
Maurizio Pierini^b, Alessandro Strumia^{d,e}

(a) *Department of Physics, University of Notre Dame, Notre Dame IN 46556, USA*

(b) *CERN, Theory Division, CH-1211 Geneva 23, Switzerland*

(c) *INFN, Laboratori Nazionali di Frascati, I-00044 Frascati, Italy*

(d) *Dipartimento di Fisica, Università di Pisa and INFN Sez. Pisa, Pisa, Italy*

(e) *National Institute of Chemical Physics and Biophysics, Tallinn, Estonia*

Abstract

We show that a right-handed stop in the 200–400 GeV mass range, together with a nearly degenerate neutralino and, possibly, a gluino below 1.5 TeV, follows from reasonable assumptions, is consistent with present data, and offers interesting discovery prospects at the LHC. Triggering on an extra jet produced in association with stops allows the experimental search for stops even when their mass difference with neutralinos is very small and the decay products are too soft for direct observation. Using a razor analysis, we are able to set stop bounds that are stronger than those published by ATLAS and CMS.

1 Introduction

Supersymmetry has been significantly cornered by LHC searches. The discovery of the Higgs boson at 126 GeV [1,2] and the direct limits on sparticles rule out most of the natural implementations of low-energy supersymmetry, at least in their simplest versions [3]. Pockets of parameter space still survive, but their exploration requires the 14-TeV phase of the LHC. At this stage, it is appropriate to examine the available experimental data and look for hints that can guide us towards special regions where supersymmetry may still hide.

In this paper, we point out that there is a window of supersymmetric parameters that *(i)* are well consistent with all collider data and flavor constraints, *(ii)* naturally emerge from RG evolution of simple UV completions, *(iii)* predict the correct thermal abundance for dark matter (DM), and *(iv)* give observable signals at LHC14. In this special window, the supersymmetric mass spectrum has the following properties:

- The lightest stop is mostly right-handed and its mass is in the range $m_{\tilde{t}_1} = 200\text{--}400$ GeV.
- The heavy, mostly left-handed, stop has a much larger mass (in the 1–2 TeV range), but it is correlated with the light stop in such a way that their geometric average is $m_S \equiv (m_{\tilde{t}_2} m_{\tilde{t}_1})^{1/2} \approx 500\text{--}600$ GeV.
- The stop trilinear term is large, such that¹ $A_t^2 \approx 6m_S^2$.
- The gluino mass is below about 1.5 TeV.
- The lightest neutralino has a mass slightly smaller than the lightest stop, by an amount of about 30–40 GeV.

In section 2 we will give several arguments that lead to the mass spectrum described above. None of them is sufficiently compelling to select conclusively the sparticle masses but these arguments, taken together, give circumstantial evidence in favor of our choice of parameters. Our conclusion is based on the following considerations:

- We choose the values of the stop parameters that minimize the average stop mass, while leading to a Higgs mass of about 126 GeV. The resulting stop mass spectrum, although not strictly natural, has the advantage of reducing the amount of unnaturalness forced upon supersymmetry by present LHC data.

¹This configuration is known as the “maximal mixing” case, although it does not necessarily imply a large mixing between the two stop mass eigenstates, as discussed in sect. 2.

- Stops affect the rates for $gg \rightarrow h$ and $h \rightarrow \gamma\gamma$. Experimental data are at present not sufficiently constraining, but will soon play an important role in selecting stop parameters. In particular, we find that stop contributions to $gg \rightarrow h$ and $h \rightarrow \gamma\gamma$ exactly cancel for $m_{\tilde{t}_2} \approx 6m_{\tilde{t}_1}$, under the conditions preferred by the Higgs mass value.
- Flavor constraints rule out a light left-handed stop, but are consistent with a light right-handed stop. We also show that, if the CKM matrix is the only source of flavor violation and the higgsino is relatively light, supersymmetric contributions can improve the agreement with the measurements of ϵ_K , while being compatible with $B \rightarrow X_s \gamma$. This is achieved for a large mass splitting between left-handed and right-handed stops.
- A large splitting between left-handed and right-handed stop masses naturally emerge from RG evolution, as long as the gluino is not too heavy. Moreover, once we require a large stop mixing parameter at low energy, we find an upper bound on the gluino mass.
- A light stop can be very helpful to obtain the right dark-matter relic density, which is typically too large for B-ino LSP or too small for higgsino or W-ino LSP in generic supersymmetric models. The process of coannihilation selects the preferred value of the mass difference between stop and neutralino.

After we have determined the favorable region for sparticle masses, we study in sect. 3 the experimental strategies for discovery at the LHC. The phenomenology of supersymmetric frameworks with light stop has been discussed at length in the recent literature (see e.g. ref. [4–9]). The search of light stops has also been the focus of recent dedicated experimental analyses by both ATLAS and CMS [10]. However, the peculiarity of our scenario is the near mass-degeneracy between stop and neutralino, which makes experimental identification especially arduous (see ref. [11–14] for previous attempts to address this problem).

On the one hand, we show that the decay $\tilde{t} \rightarrow N b \ell \nu_\ell$, which has been neglected in the present exclusive experimental searches, can dominate over the more traditional decay $\tilde{t} \rightarrow c N$, especially if the mass difference between \tilde{t} and N is not too small. The four-body decay process has the advantage of producing observable leptons in the final state, leading to a possibly higher signal/background ratio in exclusive searches. On the other hand, by an explicit simulation of this decay channel and the analysis of presently available data, we show that the inclusive searches, and particularly the CMS razor analysis, already provides significant constraints on this framework.

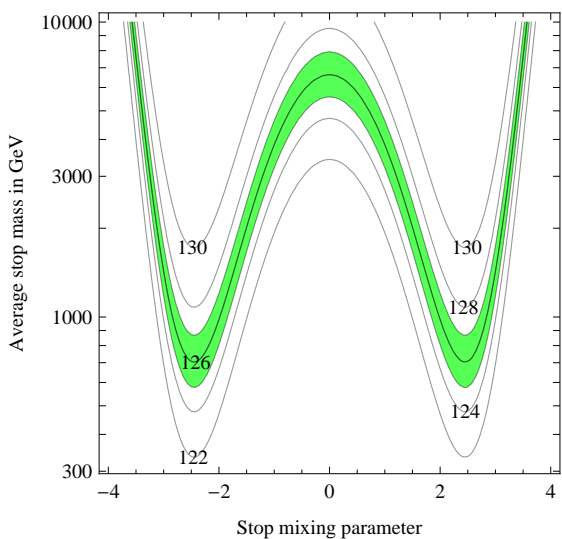


Figure 1: The Higgs mass in low-energy supersymmetry for large $\tan\beta \approx 20$. The shaded region in the (X_t, m_S) plane corresponds to the observed value of m_h . Higher-order corrections and the uncertainty in the top mass amount to an error of a few GeV in m_h .

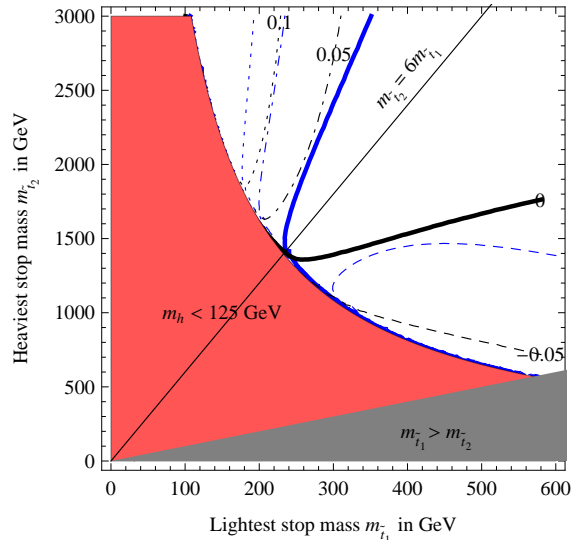


Figure 2: The white region is the range in the $(m_{\tilde{t}_1}, m_{\tilde{t}_2})$ plane allowed by the m_h constraint, while shaded regions are excluded. The full, dashed, and dotted lines correspond to fixed values of Δ_t , satisfying the m_h constraint with $|X_t| > \sqrt{6}$ (blue) or $|X_t| < \sqrt{6}$ (black).

2 The light-stop window

2.1 Constraints from the Higgs mass and decay rates

The leading part of the supersymmetric prediction for the mass of the lightest Higgs boson is

$$m_h^2 = m_Z^2 \cos^2 2\beta + \frac{3y_t^2 m_t^2}{4\pi^2} \left[\log \left(\frac{m_S^2}{m_t^2} \right) + X_t^2 \left(1 - \frac{X_t^2}{12} \right) \right] + \dots \quad (1)$$

where $X_t = (A_t + \mu \cot \beta)/m_S$, $m_S^2 = m_{\tilde{t}_1} m_{\tilde{t}_2}$ is the average stop mass, $y_t = m_t/v$ is the top-quark Yukawa coupling, and $v \approx 174$ GeV is the Higgs vev. In fig. 1 we show the region of the (X_t, m_S) plane compatible with the observed Higgs mass (for $\tan\beta \gg 1$), including also the leading two-loop corrections to the Higgs mass not shown in eq. (1). The lightest average stop mass that can lead to the observed Higgs mass is obtained for

$$m_S \approx 500 \text{ GeV} \quad \text{and} \quad X_t^2 \approx 6. \quad (2)$$

We focus on such configuration, the so-called “maximal mixing” case, since it reduces the fine-tuning in electroweak symmetry breaking and can lead to observable signals.

Further constraints on X_t and the stop masses can be obtained by examining the corrections to the $h \rightarrow \gamma\gamma$ and $h \leftrightarrow gg$ rates:

$$\frac{\Gamma(h \leftrightarrow gg)}{\Gamma(h \leftrightarrow gg)_{\text{SM}}} = (1 + \Delta_t)^2, \quad \frac{\Gamma(h \rightarrow \gamma\gamma)}{\Gamma(h \rightarrow \gamma\gamma)_{\text{SM}}} = (1 - 0.28\Delta_t)^2, \quad (3)$$

where, in the limit in which we decouple the pseudoscalar Higgs, we find

$$\Delta_t \approx \frac{m_t^2}{4} \left(\frac{1}{m_{\tilde{t}_1}^2} + \frac{1}{m_{\tilde{t}_2}^2} - \frac{X_t^2}{m_S^2} \right). \quad (4)$$

Present data (fitted in the context of the SM plus light stops) give [15]

$$\Delta_t = -0.04 \pm 0.11 \quad (5)$$

and do not yet imply a significant constraint, as it is clear from fig. 2 where we plot iso-curves of Δ_t after imposing the m_h requirement. The situation will improve in the future. Note that no deviations from the SM ($\Delta_t \approx 0$) are obtained for $m_{\tilde{t}_2} \approx 6m_{\tilde{t}_1}$ if we insist on having $X_t^2 \approx 6$.

A few comments are in order:

- An independent indication of a large splitting between $m_{\tilde{t}_2}$ and $m_{\tilde{t}_1}$ can be obtained if we assume that A_t is not significantly larger than the trace of the stop mass matrix. Assuming $A_t^2 < a(m_{\tilde{t}_1}^2 + m_{\tilde{t}_2}^2)$, then (for large $\tan\beta$) X_t^2 is bounded by

$$X_t^2 < a \frac{m_{\tilde{t}_1}^2 + m_{\tilde{t}_2}^2}{m_{\tilde{t}_1} m_{\tilde{t}_2}} \stackrel{r \ll 1}{\simeq} \frac{a}{r}, \quad r = \frac{m_{\tilde{t}_1}}{m_{\tilde{t}_2}}. \quad (6)$$

Vacuum stability arguments imply $a < 3$ (assuming $m_{H_u}^2 \ll m_{\tilde{t}_2}^2$), but this does not allow us to deduce a significant constraint on r . However, if $a \lesssim 1$ (as naturally expected from RG arguments, see next section) then we are forced to assume small values of r in order to reach $X_t^2 \approx 6$.

- Despite the large value of X_t , the mixing of the two stop eigenstates is suppressed in the limit $r \ll 1$:

$$\theta_t = \frac{1}{2} \arcsin \left(\frac{2m_t m_S X_t}{m_{\tilde{t}_2}^2 - m_{\tilde{t}_1}^2} \right) \stackrel{r \ll 1}{\simeq} \frac{r X_t m_t}{m_S}. \quad (7)$$

So, in this limit, we can approximately identify the two mass eigenstates with the electroweak eigenstates. As we will show in the next section, it is natural to identify the lightest state with an almost right-handed stop. Note also that for $r \ll 1$ the lightest stop mass is significantly lighter than the average stop mass in eq. (2): $r \approx 1/6$ corresponds to $m_{\tilde{t}_1} \approx 200$ GeV.

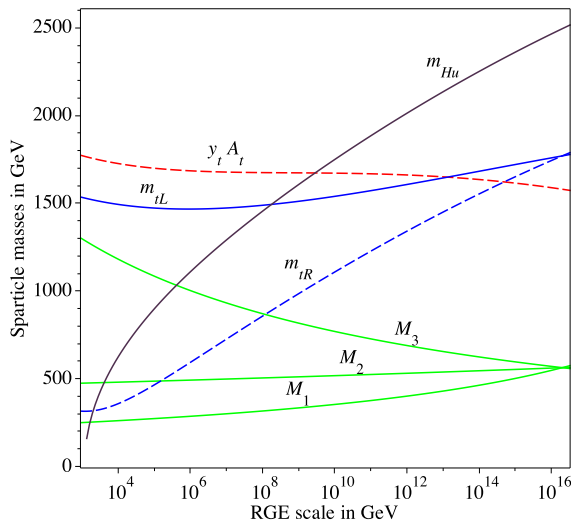


Figure 3: Illustrative example of renormalization group evolution from the unification scale to the weak scale of gaugino masses M_1 , M_2 , M_3 (green curves), of the stop mass parameters $m_{\tilde{t}_L}$ and $m_{\tilde{t}_R}$ (full and dashed blue curves, respectively), $y_t A_t$ (red dashed curve), m_{H_u} (black curve), in a configuration leading to $m_{\tilde{t}_R} \ll m_{\tilde{t}_L}$ at the weak scale. All masses are in GeV units and we assumed the MSSM.

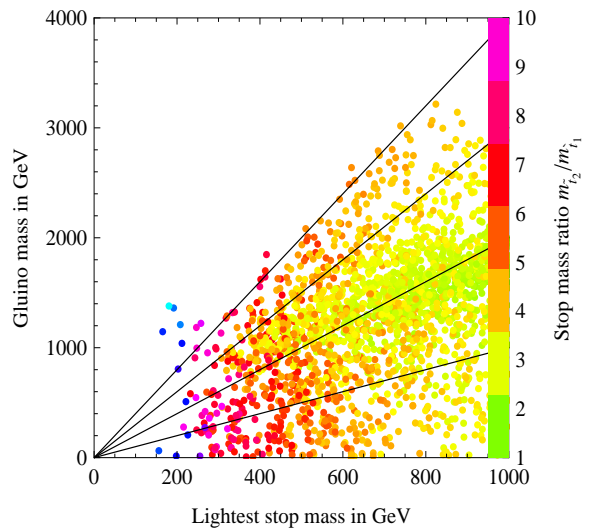


Figure 4: Gluino and light-stop masses resulting from a scan of the parameter space assuming universal scalar and gaugino masses, and the condition $|A_t| < 3m_0$, at the GUT scale. All points satisfy the $m_h \approx 126$ GeV constraint and are colored according to the value of $m_{\tilde{t}_2}/m_{\tilde{t}_1}$, as indicated on the right-handed axis. For illustrative purposes lines corresponding to $M_3/m_{\tilde{t}_1} = 1, 2, 3, 4$ are also shown.

2.2 Constraints from the RG evolution

A numerically large splitting between $m_{\tilde{t}_L}$ and $m_{\tilde{t}_R}$ naturally arises from the evolution under renormalization-group equations (RGE), provided scalar masses are significantly larger than gaugino masses at the high scale [17]. This can be understood by looking at the one-loop RGE for third generation squark masses and m_{H_u} . Neglecting off-diagonal flavor-mixing terms we have

$$8\pi^2 \frac{dm_{\tilde{t}_L}^2}{d \log \mu} = y_t^2 Y_t - \frac{16}{3} g_3^2 M_3^2 - 3g_2 M_2^2 - \frac{1}{15} g_1^2 M_1^2, \quad (8)$$

$$8\pi^2 \frac{dm_{\tilde{t}_R}^2}{d \log \mu} = 2 y_t^2 Y_t - \frac{16}{3} g_3^2 M_3^2 - \frac{16}{15} g_1^2 M_1^2, \quad (9)$$

$$8\pi^2 \frac{dm_{H_u}^2}{d \log \mu} = 3 y_t^2 Y_t - 3g_2 M_2^2 - \frac{3}{5} g_1^2 M_1^2, \quad (10)$$

where μ is the renormalization scale, and

$$Y_t = m_{\tilde{t}_L}^2 + m_{\tilde{t}_R}^2 + m_{H_u}^2 + A_t^2. \quad (11)$$

The RG evolution of the stop masses depends mainly on two effects: the QCD term ($g_3^2 M_3^2$) and the Yukawa term ($y_t^2 Y_t$). If we take M_3 , $m_{\tilde{t}_L}$ and A_t to be comparable and in the range 1–2 TeV at the weak scale (in order to fulfill the m_h constraints and the experimental bounds on the gluino mass), we find that: i) QCD and Yukawa terms compensate to a large extent in the running of $m_{\tilde{t}_L}$; ii) the Yukawa term is dominant during most of the running of $m_{\tilde{t}_R}$, leading to $m_{\tilde{t}_R} \ll m_{\tilde{t}_L}$ at the weak scale starting from the initial condition $m_{\tilde{t}_R} = m_{\tilde{t}_L}$ at some high scale; iii) the Yukawa term is always dominant in the running of $m_{H_u}^2$, which naturally becomes negative at the weak scale.

An illustrative spectrum is shown in fig. 3a, where we required $m_{H_u}^2 = -m_Z^2/2$, $M_3 = 1.3$ TeV, and $m_{\tilde{t}_R} < 300$ GeV at the weak scale, and adjusted A_t in order to achieve the condition $m_{\tilde{t}_R} = m_{\tilde{t}_L}$ at 2×10^{16} GeV. The corresponding weak-scale configuration is consistent with all the existing experimental bounds, with the condition $m_h = 126$ GeV (assuming $\tan \beta \gtrsim 5$), and with a light stop below 300 GeV. A few percent tuning in the initial values of $m_{H_u}^2$ and the higgsino mass μ is necessary in order to achieve the correct pattern of electroweak symmetry breaking, but this is unavoidable in the minimal supersymmetric model with $m_h = 126$ GeV. The soft-breaking terms needed to reach this low-energy configuration require an initial splitting $m_{\text{squarks}}^2/m_{\text{gauginos}}^2 \sim 10$ at the high-energy scale. All three generations of squarks can be degenerate at the high scale, since the separation of the right-handed stop is fully driven by the dynamics of the low-energy degrees of freedom. In this case the squarks of the first two generations would have a mild RGE evolution (reaching low-energy values slightly above 2 TeV for the illustrative configuration shown in fig. 3a).

The dynamical separation between $m_{\tilde{t}_R}$ and $m_{\tilde{t}_L}$, together with the generation of a large X_t , from high-scale RG running naturally occurs only in a limited range of gluino masses. This can be understood by inspecting the expressions of A_t , $m_{\tilde{t}_R}$ and $m_{\tilde{t}_L}$ at the weak scale in models with a universal scalar mass m_0 and trilinear coupling A_0 at the GUT scale,

$$A_t \approx 0.3A_0 + 0.8M_3, \quad (12)$$

$$m_{\tilde{t}_R}^2 \approx 0.5M_3^2 - 0.07A_0^2 - 0.10A_0M_3 + 0.3m_0^2, \quad (13)$$

$$m_{\tilde{t}_L}^2 \approx 0.7M_3^2 - 0.03A_0^2 - 0.05A_0M_3 + 0.7m_0^2, \quad (14)$$

where M_3 is the gluino mass at the weak scale. From these equations it is clear that if $M_3 \ll m_0$, $|A_0|$ a large splitting among the two stop masses and a large X_t are obtained only for unnaturally large values of $|A_0|/m_0$. Similarly, maximal mixing and large splitting cannot be obtained if $M_3 \gg m_0$, $|A_0|$. The upper bound on M_3 , which is particularly important for the LHC searches, is quantified in fig. 4, where we show the points satisfying the m_h constraint in the $m_{\tilde{t}_1}$ – M_3 plane. As can be seen, the gluino must satisfy the approximate

upper bound $M_3 \lesssim 4m_{\tilde{t}_1}$, that implies $M_3 \lesssim 1.6$ TeV for the range of $m_{\tilde{t}_1}$ ($m_{\tilde{t}_1} \lesssim 400$ GeV) corresponding to a large $m_{\tilde{t}_2}/m_{\tilde{t}_1}$ ratio.

As anticipated, in this framework $m_{H_u}^2$ naturally becomes negative at the weak scale and the μ term must be properly adjusted to reproduce the correct value of m_Z . Assuming universal scalar masses at the high scale, $m_{H_u}^2$ runs very negative at the weak scale, implying $|\mu| > m_{\tilde{t}_R}$, or heavy higgsinos. Alternatively, we can consider a scenario as in fig. 3, with non-universal boundary conditions, where $|\mu| < m_{\tilde{t}_R}$ and thus higgsinos are lighter than the right-handed stop. The two cases lead to a rather different phenomenology for flavor, dark matter, and LHC searches.

2.3 Constraints from flavor physics

If some of the gauginos or higgsinos are not too heavy, a light stop can have a significant impact on low-energy flavor-physics observables. On general grounds, even if gauginos and higgsinos are in the several-TeV domain, sizable misalignments in flavor space between quark and squark mass matrices are excluded. Therefore we assume that the light stop is mostly right-handed and aligned in flavor space with the top quark. The remaining flavor violation is described by the usual CKM angles in charged currents. An interesting and largely model-independent correlation (controlled only by the size of $|\mu|$ and the stop mass parameters) emerges between $\text{BR}(B \rightarrow X_s \gamma)$ and ϵ_K .

In the limit in which we retain only the effect of higgsinos and flavor-aligned right-handed stop, the deviations from the SM in these two observables are described by

$$\frac{\text{BR}(B \rightarrow X_s \gamma)}{\text{BR}(B \rightarrow X_s \gamma)_{\text{SM}}} = 1 - 2.5 \Delta C_7 - 0.7 \Delta C_8, \quad (15)$$

$$\frac{\epsilon_K}{\epsilon_K^{\text{SM}}} = 1 + 1.9 \frac{m_t^2}{m_{\tilde{t}_R}^2} F_2 \left(\frac{\mu^2}{m_{\tilde{t}_R}^2} \right), \quad (16)$$

where

$$\Delta C_{7,8} = \sin \theta_t \tan \beta \frac{\mu m_t}{m_{\tilde{t}_R}^2} F_{7,8}^{\text{LR}} \left(\frac{\mu^2}{m_{\tilde{t}_R}^2} \right) + \frac{m_t^2}{m_{\tilde{t}_R}^2} F_{7,8}^{\text{RR}} \left(\frac{\mu^2}{m_{\tilde{t}_R}^2} \right), \quad (17)$$

and the normalization of the various loop functions (see Ref. [16, 18] for the explicit expressions) is

$$F_7^{\text{LR}}(1) = -\frac{2}{9}, \quad F_8^{\text{LR}}(1) = -\frac{1}{12}, \quad F_7^{\text{RR}}(1) = \frac{5}{144}, \quad F_8^{\text{RR}}(1) = \frac{1}{48}, \quad F_2(1) = \frac{1}{12}. \quad (18)$$

For $B \rightarrow X_s \gamma$ we have expanded the result to first order in the stop-mixing angle. Note that, even for $|\sin \theta_t| \ll 1$, the first term in eq. (17) can be sizable and can dominate over

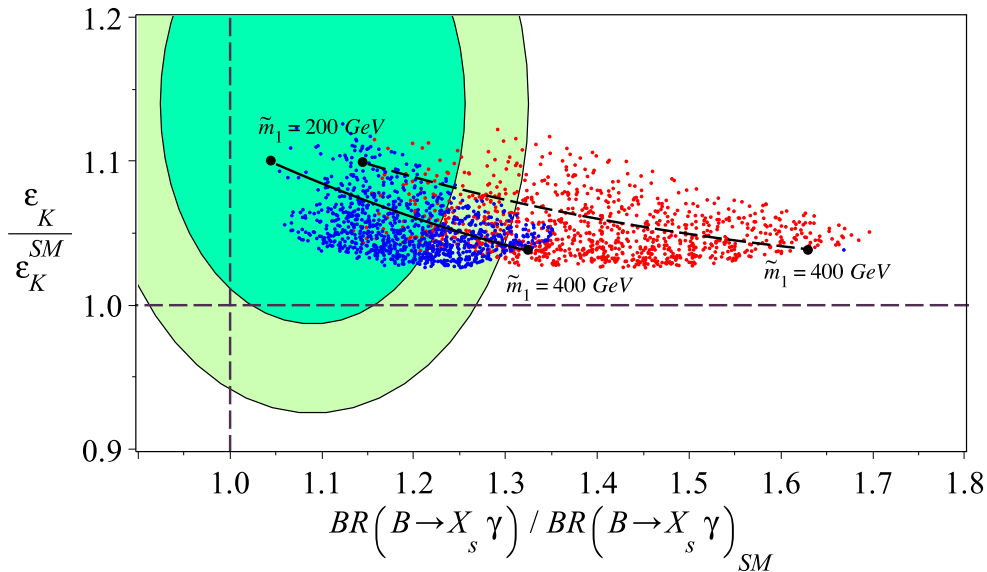


Figure 5: Correlation between $BR(B \rightarrow X_s \gamma)$ and ϵ_K . The two ellipses denote the 68% and 90% CL experimental range. All points reproduce the observed Higgs mass. The two black curves are obtained varying $m_{\tilde{t}_R}$ between 200 GeV and 400 GeV (from left to right) for $m_S = 500$ GeV, $\mu = 250$ GeV, and $\tan \beta = 20$ (dashed curve) or $\tan \beta = 10$ (full curve). The points are obtained varying the parameters in the range $\mu = [150 - 400]$ GeV and $m_{\tilde{t}_R} = [200 - 400]$ GeV, with $m_S < 700$ GeV and $\tan \beta = 20$ (red) or $\tan \beta = 10$ (blue).

the second one, both because of the large value of the loop function F_7^{LR} and because the m_h constraint favors $\tan \beta \gg 1$. As a result, the experimental constraint on $BR(B \rightarrow X_s \gamma)$ puts a very stringent bound on the maximal value of $|\theta_t|$ for higgsino masses of $O(m_{\tilde{t}_R})$, providing a further argument in favor of a sizable hierarchy between the two stop mass eigenstates [see eq. (7)]. The sign of the correction can be positive or negative, depending on the relative sign of μ and A_t . The experimental data favor a constructive interference with the SM amplitude: $BR(B \rightarrow X_s \gamma)_{\text{exp}}/BR(B \rightarrow X_s \gamma)_{\text{SM}} = 1.09 \pm 0.11$.²

In the case of ϵ_K , the correction is always positive and, in first approximation, is independent from the mixing angle. As a result, the present experimental constraint $\epsilon_K^{\text{exp}}/\epsilon_K^{\text{SM}} = 1.14 \pm 0.10$ [22] can be better satisfied if μ is not too heavy.

The correlation between the two observables is shown in fig. 5, where we restrict the attention to the value of $\text{sgn}(\mu A_t)$ favored by $BR(B \rightarrow X_s \gamma)$. As can be seen, after imposing the m_h constraint and requiring $|\mu| \lesssim 400$ GeV, present data favor the configuration with

²This ratio is evaluated using the SM estimate from Ref. [19], and a naive average of the HFAG result and the latest Babar result [21] on $BR(B \rightarrow X_s \gamma)_{\text{exp}}$.

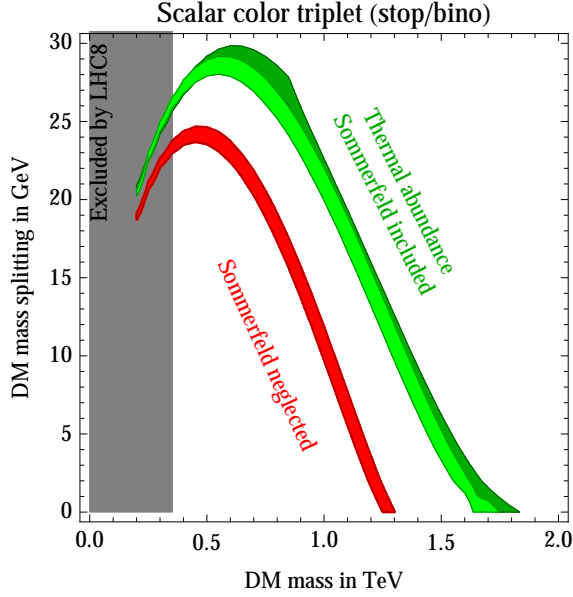


Figure 6: Points in the supersymmetric parameter space that lead to the correct DM abundance.

$m_{\tilde{t}_R} \ll m_{\tilde{t}_L}$ that maximizes the correction to ϵ_K and minimizes the impact in $\text{BR}(B \rightarrow X_s \gamma)$.

2.4 Constraints from dark matter

A light stop offers the opportunity of curing the excessive relic abundance of B-ino LSP, generally encountered in supersymmetric models. Indeed, the DM cosmological abundance can be reproduced with a B-ino thermal relic that co-annihilates with stops if

$$m_{\tilde{t}_1} = M_{\text{DM}} + \Delta M \quad \text{with} \quad \Delta M \approx 30 \text{ GeV}. \quad (19)$$

The relatively small mass difference arises imposing that the average annihilation cross section equals

$$\sigma v_{\text{cosmo}} \equiv (2.3 \pm 0.1) \times 10^{-26} \text{ cm}^3 \text{ s}^{-1} \quad (20)$$

at the freeze-out temperature $T_f \approx M_{\text{DM}}/25$. The dominant annihilation process is s -wave stop annihilation into gluons (annihilation into quarks is p -wave suppressed):

$$\sigma(\tilde{t}_1 \tilde{t}_1^* \rightarrow gg)v = \frac{7 g_3^4}{432 \pi m_{\tilde{t}_1}^2}. \quad (21)$$

Averaging over the components of the DM system (\tilde{t} and \tilde{t}^* have 3 colors each, and the neutralino has 2 polarisations) we get

$$\sigma v_{\text{cosmo}} = \sigma(\tilde{t}_1 \tilde{t}_1^* \rightarrow gg)v \times \left[1 + \frac{e^{\Delta M/T}}{3(1 + \Delta M/M)^{3/2}} \right]^{-1}. \quad (22)$$

The region where the DM abundance reproduces the cosmological values within 3 standard deviations is shown as a red band in fig. 6 (see also [25]). In the figure we also show, as green band, the result of a more precise computations that takes into account strong Sommerfeld corrections [24].

3 Experimental signals

3.1 Stop decay rates

Beside gluino production, the most characteristic signal comes from the (mostly right-handed) light stop. Dark matter considerations motivate the searches for a stop that is near degenerate with the neutralino LSP, with a mass difference $\Delta M \equiv m_{\tilde{t}_1} - M_{\text{DM}} \approx 30 \text{ GeV}$. In this configuration, the stop is usually assumed to decay according to $\tilde{t}_1 \rightarrow cN$. Here we point out that four-body stop decays (not suppressed by flavor-changing neutral currents) can easily become competitive with the two-body flavor-violating decay. In the limit of small ΔM , the relevant stop decay widths are

$$\Gamma(\tilde{t}_1 \rightarrow cN) = \frac{2g^2 \tan^2 \theta_W \theta_{tc}^2 \Delta M^2}{9\pi m_{\tilde{t}_1}} = 100 \text{ cm}^{-1} \left(\frac{\theta_{tc}}{10^{-5}} \right)^2 \left(\frac{\Delta M}{30 \text{ GeV}} \right)^2 \left(\frac{400 \text{ GeV}}{m_{\tilde{t}_1}} \right), \quad (23)$$

$$\Gamma(\tilde{t}_1 \rightarrow Nbl^+\nu_\ell) = \frac{3g^6 \tan^2 \theta_W \Delta M^8}{70(6\pi)^5 M_W^4 m_t^2 m_{\tilde{t}_1}} = 28 \text{ cm}^{-1} \left(\frac{\Delta M}{30 \text{ GeV}} \right)^8 \left(\frac{400 \text{ GeV}}{m_{\tilde{t}_1}} \right), \quad (24)$$

as well as

$$\Gamma(\tilde{t}_1 \rightarrow Nbu\bar{d}) \approx \Gamma(\tilde{t}_1 \rightarrow Nbc\bar{s}) \approx 3\Gamma(\tilde{t}_1 \rightarrow Nbl^+\nu_\ell) \quad \ell = e, \mu, \tau. \quad (25)$$

For the decay $\tilde{t}_1 \rightarrow cN$, the parameter θ_{tc} is the effective stop–charm mixing angle. In general, θ_{tc} is a free unknown parameter, since it depends on the flavor structure of the soft terms. Assuming that it vanishes at some high scale Λ_{UV} , a non zero value is generated by RGE effects due to the SM Yukawa couplings (even in absence of other sources of flavor violation) [26]. In our scenario, where $\tilde{t}_1 \approx \tilde{t}_R$, the leading effect comes from an induced \tilde{t}_R – \tilde{c}_L mixing, which can be estimated as

$$\theta_{tc}^{\text{MFV}} \sim \frac{y_t y_b^2 V_{cb} V_{tb}^* v A}{16\pi^2 \tilde{m}^2} \log \frac{\Lambda_{\text{UV}}}{\tilde{m}} = 3 \times 10^{-5} \left(\frac{2 \text{ TeV}}{\tilde{m}} \right) \left(\frac{\log \Lambda_{\text{UV}}/\tilde{m}}{30} \right) \left(\frac{\tan \beta}{10} \right)^2, \quad (26)$$

where we have omitted $\mathcal{O}(1)$ loop functions depending on mass ratios of heavy squarks and charginos, whose average mass is denoted by \tilde{m} .

The $\tilde{t}_1 \rightarrow Nbl^+\nu_\ell$ decay receives contributions suppressed by heavy sparticles or mediated only by virtual SM particles. We here focus on the latter contribution, which is dominant in our case. This leads to eq. (24), whose derivation is given in the appendix, together with the matrix element relevant for implementation in Monte Carlo codes.

The two decay channels can dominate in different regions of the parameter space and become roughly comparable for $\theta_{tc} \sim 10^{-5}$ and stop–neutralino mass differences motivated by DM considerations. However, the large model dependence of θ_{tc} prevents us from making any firm conclusion. The four-body decay has a much steeper dependence on ΔM and becomes less relevant for very small ΔM . The decay $\tilde{t}_1 \rightarrow Nbl^+\nu_\ell$, not previously considered in the literature, is interesting from the experimental point of view since it leads to an additional soft lepton.

Since the $\tilde{t}_1 \rightarrow cN$ decay only produces an unobservable soft jet and its signatures have been previously studied, in the following we focus our attention mainly on the four-body decay channels in eqs. (24)–(25), which we assume to be the dominant decay modes. As we discuss below, the bounds we are able to derive at present from existing LHC searches are largely independent from this assumption; however, the presence of a lepton in the final state could possibly lead to stringent bounds with future optimized searches (see sect. 3.3). Assuming the four-body modes to be dominant implies

$$\text{BR}(\tilde{t}_1 \rightarrow Nbl^+\nu_\ell) \approx 1/9 \quad (27)$$

for each lepton flavor ℓ . Moreover, the smallness of the total decay width implies that the decay vertex displacement may be detectable.

3.2 Bounds from existing LHC searches

The challenge of detecting stop decays for compressed spectra is all in the capability of reconstructing and identifying the soft decay products of the two stop decays. On the other hand, this is not the only experimental handle we have.

The first problem is with triggering these events. The jets and leptons originating from the stop decay are too soft to be used to retain the events during on-line selection, given the (CPU and bandwidth) budget of the experiments. The only possibility is to detect these processes through the associate jet production ($\tilde{t}\tilde{t}^*$ plus one or more jets), with a consequent reduction of the effective cross section.

In the worst case scenario, all the decay products are lost and one is left with one or more

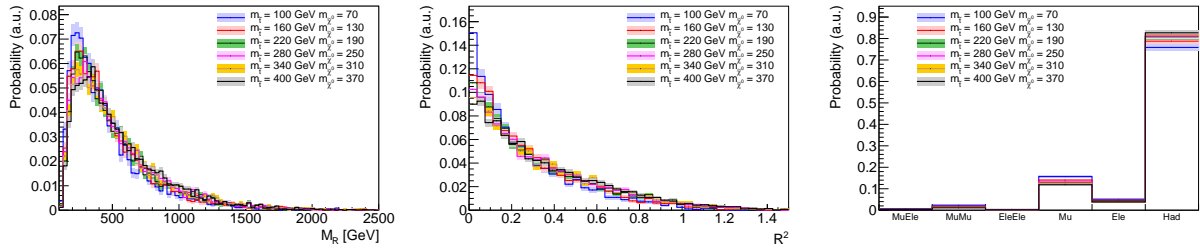


Figure 7: *Distribution of M_R (left), R^2 (center), and box-by-box event fraction (right) for pair-produced stop events as a function of the stop mass, for $\tilde{t} \rightarrow l\nu_\ell bN$ decays and $m_{\tilde{t}} - M_{\text{DM}} = 30$ GeV. Even if this case is the most favorable for the selection of leptonic final states, the hadronic box is the most populated due to the small value of $m_{\tilde{t}} - M_{\text{DM}}$.*

jets: bounds exist from monojet searches [27,28] (performed in the Dark Matter context) and from searches with ≥ 2 jets [29,31] (performed in supersymmetric contexts); see also [30].

In the best case scenario one can also detect the leptons from the decay of the stop pair. This is why it is interesting to consider a set of analyses that focus on ≥ 2 jets for events with or without leptons. The CMS razor analysis [32,33] is a all-in-one answer to our needs, with the additional advantage that the jet selection in the analysis is looser than the one used in the hadronic SUSY searches: $p_T^{\text{jet}} > 60$ GeV for the first two jet; $p_T^{\text{jet}} > 40$ for the other jets. The looser jet selection increases the effective cross section we are sensitive to.

To estimate the sensitivity of the search to the soft leptons from the stop decays, we implemented an emulation of the razor analysis, based on generator-level jets and leptons. We generate pair-produced stop squarks in $\sqrt{s} = 7$ TeV pp collisions using PYTHIA8 [34]. The stop are forced to decay with a flat matrix element as $\tilde{t} \rightarrow l\nu_\ell bN$. The transverse momenta of all the visible particles are summed to compute the missing transverse energy at generator level. Similarly, these particles are clustered into jets using the FASTJET [35,36] implementation of the antikT [37] algorithm. As for CMS, we use $R = 0.5$ to define the jet size. The razor variables and the six *boxes* (MuEle, MuMu, EleEle, Mu, Ele, and Had) are defined following the instructions provided by the CMS collaboration [38]. To take into account the limited efficiency in lepton detection, we applied the efficiency curves of the CMS dilepton SUSY search [39], using a hit-or-miss analysis. This is a valid procedure, since the lepton definition in the razor and dilepton SUSY searches are similar.

We scan the value of the stop mass between 100 GeV and 400 GeV, fixing the stop-to-neutralino mass gap to 30 GeV. We show in fig. 7 the distribution of the razor variables for different stop masses, as well as the breakdown in boxes. A few important features should be noticed:

- i) The M_R variable approximates the momentum of the jets in the frame such that $|p_{j_1}| = |p_{j_2}|$. In the case of squark pair-production, for which this variable was designed, this corresponds to the squarks rest frame. This is why the M_R distribution for this case peaks at the $M_\Delta = (m_{\tilde{t}_1}^2 - M_{\text{DM}}^2)/m_{\tilde{t}_1}$. Instead, in the case we consider here the jets come from the associated (non-resonant) production and the peak is at ~ 150 GeV, regardless of the stop and neutralino masses (due to the selection on the jet p_T and not to the SUSY kinematic).
- ii) The R variable is defined as M_R^T/M_R where $M_R^T \leq M_\Delta$ is a transverse invariant mass, such that the QCD background peaks at $R \sim 0$, while the signal can produce events with larger values of R , where the two jets have similar directions, opposite to the direction of the neutralinos. In the case of compressed stop spectra the R^2 distribution has some dependence on the stop mass, due to the correlation between the stop mass (setting the scale of the hard interaction), the spectrum of the associated jets, and the missing energy in the event.
- iii) The majority of the events selected by the analysis falls in the hadronic box.

All these features are explained by the fact that the analysis is only sensitive to the events with two associated jets. These jets form the hemispheres and the razor variables are computed for a *non-resonant* production. In the largest fraction of the events the decay products of the stop are not seen and, effectively, the signal behaves like for the direct production of Dark Matter [40], The stop plays the part of the Dark Matter, with the big advantage of the production cross section much larger than for Dark Matter direct detection. At the same time, the result is largely independent on the final state the stop decays to.

These considerations suggest that the Had box is the only relevant sample to consider in our study. This is also the only box for which the information needed for phenomenology studies (observed yield and expected background vs R^2 and M_R) are given (the number of expected background events is shown in fig. 8). While we limit our study to the Had box, we stress the fact that there is some sensitivity in the Mu box and Ele boxes, which could have be exploited if we had the relevant information. The importance of the Had box over the others also implies that the monojet analysis is a good candidate to look for our signal, as it is for Dark Matter direct production. The

We show in fig. 9 the limits obtained with the monojet and the razor (Had-only) analyses. For both the analyses, we consider the expected background yield (with error) and the observed yield, and we model the likelihood according to a Poisson distribution. The background uncertainty is described using a log-normal function. We assign a 30% error

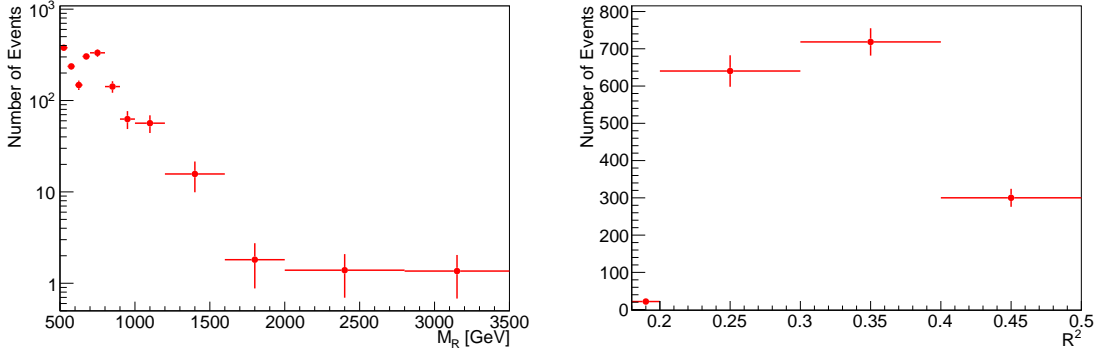


Figure 8: Projections of the expected background in the razor hadronic box, obtained from the bin-by-bin expected background in the $\sqrt{s} = 7$ TeV run of CMS (from ref. [33, 38]).

to the signal efficiency, to take into account the differences between our implementation of the analysis and a more realistic description of the CMS detector. We then derive a posterior-probability density function for the signal cross section as:

$$P(\sigma) = \int_0^\infty db \int_0^1 d\epsilon \frac{(b + L\sigma\epsilon)^n e^{-b-L\sigma\epsilon}}{n!} \text{Ln}(\epsilon|\bar{\epsilon}, \delta_\epsilon) \text{Ln}(b|\bar{b}, \delta_b) \quad (28)$$

where b (ϵ) is the actual value for the background yield (the efficiency), \bar{b} ($\bar{\epsilon}$) is its expected value, and δ_b (δ_ϵ) the associated error; $\text{Ln}(x|m, \delta)$ is a log-normal function for x with mean m and variance σ ; n is the observed yield, L is the available luminosity (for which we neglect the $\sim 4\%$ error) and σ is the signal cross section. In the case of the razor analysis, the actual posterior is obtained as the product of the posteriors in each of the bins provided in [38]. We verified that taking $L = \epsilon = 1$ we can reproduce the limit on the signal strength for the two analyses. The 95%-probability limit is obtained integrating the posterior from 0 up to the value σ_{UP} such that

$$\frac{\int_0^{\sigma_{\text{UP}}} P(\sigma) d\sigma}{\int_0^\infty P(\sigma) d\sigma} = 0.95. \quad (29)$$

The left plot of fig. 9 shows the 95%-probability limit on the signal cross section as a function of the stop mass for both the analyses, fixing the mass split at 30 GeV and 100 GeV (with the stop decayed to t^*N). The sensitivity of the monojet analysis is limited by the tight selection on jets and missing transverse energy. The limit is worse for larger splitting because of the veto on any third jet with $p_T > 30$ GeV. At the contrary, the razor analysis is more efficient for this signature and more performant for larger splitting, since no veto is applied. One should also consider that at large values of the mass splitting the five leptonic boxes could further improve the sensitivity.

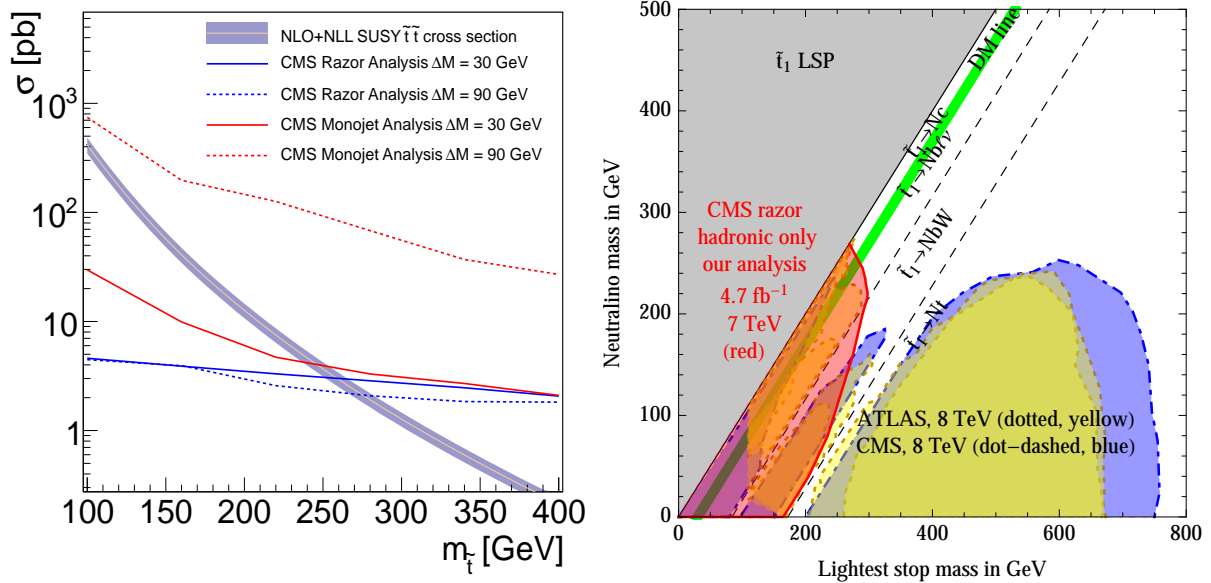


Figure 9: **Left:** predicted cross section and experimental limits as functions of the lightest stop mass. **Right:** excluded regions in the $(m_{\tilde{t}_1}, M_{DM})$ plane from our re-analysis of 7 TeV data (red) compared with latest ATLAS (dotted regions shaded in yellow) and CMS (dot-dashed regions shaded in green) analyses of 8 TeV data.

The right plot of fig. 9 shows the limit in the stop mass vs neutralino mass plane. This plot shows the same qualitative features as the 1D limit plot. At large splits, the limit from the razor analysis is found to be consistent with (and slightly worse than) the official limit on stop pair production [33]. Both the 1D and 2D limits were obtained comparing the excluded cross section with the NLO+NLL $\tilde{t}\tilde{t}^*$ cross section at 7 TeV taking the decoupling limit for the other SUSY particles [41].³

3.3 Dedicated analyses

The existing limit is interesting, considering how challenging this signature is. This study also shows once more that the inclusive searches by ATLAS and CMS are much more general than the signal signatures they have been designed for. While a dedicated search could do better for a specific scenario, the inclusive searches are a good assurance policy for unexpected signatures. Repeating the analysis at 8 TeV with more data will certainly push the sensitivity further. On the other hand, we think it is interesting to imagine how the analyses could be

³In the revised version of the plot (september 2014) we subtract the signal contribution in the sideband to the background estimate by CMS. This effect, generically negligible in the models considered by the original analysis, becomes relevant in our study for large values of the stop-neutralino mass splitting. Furthermore, we plot the latest bounds from ATLAS and CMS with 8 TeV data.

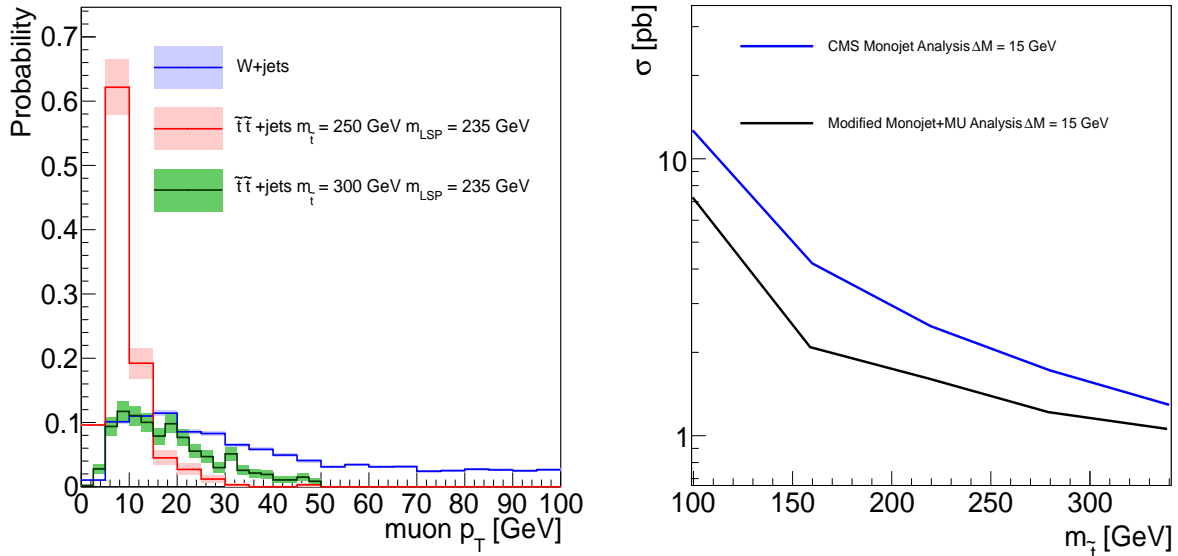


Figure 10: *Improvements that can be obtained with a dedicated search. Left: distribution of the muon p_T for W +jets and stop-pair events passing the CMS monojet selection criteria, except for the muon veto and the veto on isolated tracks. Right: expected excluded cross section for stop pair production obtained from the CMS monojet analysis (blue) and a modified monojet+muon search (black). Events are generated with four-body stop decays to $f\bar{f}'bN$, of which $\sim 20\%$ produce one muon.*

changed to improve the sensitivity.

One could certainly gain by using looser kinematic requirements. The limiting factor is related to the triggers. For example, it was pointed out extending the razor analysis at the tail of R^2 for low M_R could improve the sensitivity to DM production [40]. The same conclusion applies to compressed stop-neutralino spectra, since the signature in the razor Had box is the same.

A change in the lepton selection could further increase the sensitivity of these analyses. The left plot on Fig. 10 shows the distribution of the muon p_T for W +jets events selected by the CMS monojet analysis, before applying the muon veto and the isolated track veto. This is compared to the equivalent distribution obtained for events with pair-produced stops, decaying to W^*bN , with at least one of the two W^* producing a $\mu\nu$ pair. We consider two values of the stop mass ($m_{\tilde{t}} = 150$ GeV and $m_{\tilde{t}} = 270$ GeV) for $\Delta M = 15$ GeV. Requiring one muon with $p_T < 15$ GeV corresponds to reducing the $Z(\nu\nu)$ +jets background to a negligible level, and to rejecting $\sim 92\%$ of the other backgrounds.

To evaluate the potential improvement due to this change, we applied the monojet anal-

ysis to the generated stop-stop samples, and we separate the selected events in two boxes (as for the razor analysis): the Muon box, including all the events with one muon with $p_T < 15$ GeV; the Had box, with all the other events. We then distribute the background in the two boxes as follows: all the $Z(\nu\nu)+\text{jets}$ background to the Had box; 8% (92%) of the other background in the Mu (Had) box. We then evaluate the potential sensitivity of this modified analysis on a sample of pair-produced stop decays, decaying to W^*bN , 20% of which produce at least one muon in stop decay.

The right plot of Fig. 10 shows the expected exclusion limit, compared to what is obtained with the usual monojet analysis. A similar improvement could be used for electrons, provided the understanding of the electron identification and the fake rate at low p_T . One should keep in mind that our results come from a simplified description of the CMS detector. A more accurate assessment of the improvement can only be obtained with a detailed simulation of the detector performances. We look forward to see this change applied to the monojet analyses by ATLAS and CMS.

As a side remark, we would like to stress the fact that the stop decay products could be displaced from the primary vertex of the proton-proton collision. Requiring a displaced vertex, particularly with one muon originating from it, can potentially reduce the standard model background to a very small level. However for $\Delta M \approx 30$ GeV only a small fraction of the \tilde{t}_1 decay after a detectable path of about 1 mm. An accurate estimate of the signal sensitivity for a displaced-vertex analysis would require an accurate description of the vertex resolution for the LHC detectors and should be investigated directly by the ATLAS and CMS collaborations. Even if the signal reduction is too large to be beneficial for 8 TeV searches, this is an interesting possibility in light of the high statistics expected for the future 14 TeV LHC run.

4 Conclusions

We have put forward a series of theoretical arguments that motivate the existence of a mainly right-handed stop in the mass range $m_{\tilde{t}_1} = 200\text{--}400$ GeV, together with a neutralino 30–40 GeV lighter and, possibly, a gluino with mass below 1.5 TeV. However, quite independently of any of these specific motivations, the search for stops nearly degenerate with the neutralino LSP is an important experimental task, necessary to cover possible corners of parameter space where supersymmetry may still hide.

We have pointed out that, when the mass splitting between stop and neutralino is smaller

than $M_W + m_b$, the previously-neglected four-body decay processes $\tilde{t}_1 \rightarrow Nbl^+\nu_\ell$ and $\tilde{t}_1 \rightarrow Nbq\bar{q}'$ can compete with the flavor-changing decay $\tilde{t}_1 \rightarrow cN$. The presence of a charged lepton in the final state of the four-body decay gives a useful handle to identify the stop in this experimentally difficult mass configuration where all visible particles are relatively soft.

Regardless of the particular stop decay mode, the request of an extra jet in association with the stop pair greatly improves triggering capability and signal identification. We have shown that the inclusive searches using razor analysis are very efficient to probe stops nearly degenerate with neutralinos. In this region of mass parameters, we are able to set limits on the stop that are stronger than those published by ATLAS and CMS. Our limits (shown in fig. 9) extend up to stop masses of about 250 GeV, even for a vanishing stop–neutralino mass difference. This means that the LHC has already started to probe the “light stop window” motivated by our theoretical considerations, but most of the interesting region will be explored only at LHC14.

Note Added

While our paper was being completed, similar results were presented in [42, 43]. In our analysis we used the response function for the CMS detector, provided by the CMS collaboration, instead of trying to emulate the LHC detectors. More importantly, we used the full likelihood provided by the CMS collaboration for the inclusive razor analysis, which gives a realistic description of the likelihood resulting from the data. This prevented us from extending our study to the razor btag search [44]. The latter has a better sensitivity in presence of bjets with $p_T > 40$ GeV (i.e. far from the diagonal of the $m_{\tilde{\chi}^0}$ vs. $m_{\tilde{t}}$ plane), if an accurate emulation of the btag efficiency and the mistag rate is reached. On the diagonal, only a small fraction of the associated jets are bjets, such that requiring a btag has the effect of reducing the expected signal much more than the factor-three background reduction.

Acknowledgments

AD was partly supported by the National Science Foundation under grants PHY-0905383-ARRA and PHY-1215979. AS was supported by the ESF grant MTT8 and by SF0690030s09 project.

Appendix

In this appendix we derive the four-body stop decay width given in eq. (24). In the limit of small mass difference ($\Delta M \ll M_W, m_t$), the amplitude for pure right-handed stop decay $\tilde{t}_R \rightarrow Nbe^+\nu$ is

$$|\mathcal{A}|^2 = \frac{32g^6 \tan^2 \theta_W}{9M_W^4 m_t^2} (P_N \cdot P_e)(P_b \cdot P_\nu) , \quad (30)$$

where P_i are the quadri-momenta of the particles involved. The decay width is given by

$$\Gamma = \int d\phi^{(4)} \frac{|\mathcal{A}|^2}{2m_{\tilde{t}}} . \quad (31)$$

The 4-body phase space integral $d\phi^{(4)}$ can be analytically performed at leading order in $\Delta M = m_{\tilde{t}} - M_{\text{DM}}$. Indeed, by writing the decay as $\tilde{t} \rightarrow XY \rightarrow (Ne)(b\nu)$, the amplitude for each sub-decay is separately Lorentz invariant. Thus, using

$$d\phi^{(4)} = \frac{ds_X ds_Y}{(2\pi)^2} d\phi^{(2)}(\tilde{t} \rightarrow XY) d\phi^{(2)}(X \rightarrow Ne) d\phi^{(2)}(Y \rightarrow b\nu) , \quad (32)$$

$$|\mathcal{A}|^2 = \frac{8g^6 \tan^2 \theta_W}{9M_W^4 m_{\tilde{t}}^2} s_X (s_Y - M_{\text{DM}}^2) , \quad (33)$$

we get

$$\Gamma = \int_{M_{\text{DM}}^2}^{m_{\tilde{t}}^2} ds_Y \int_0^{(m_{\tilde{t}} - \sqrt{s_Y})^2} ds_X \left(1 - \frac{M_{\text{DM}}^2}{s_Y} \right) \frac{\lambda(m_{\tilde{t}}^2, s_X, s_Y) |\mathcal{A}|^2}{4(4\pi)^5 m_{\tilde{t}}^3} = \frac{2g^6 \tan^2 \theta_W I}{9(4\pi)^5 M_W^4 m_{\tilde{t}}^2 m_{\tilde{t}}} , \quad (34)$$

$$I \equiv m_{\tilde{t}}^8 \int_{M_{\text{DM}}^2/m_{\tilde{t}}^2}^1 dy \int_0^{(1-\sqrt{y})^2} dx \frac{x}{y} \left(y - \frac{M_{\text{DM}}^2}{m_{\tilde{t}}^2} \right)^2 \sqrt{(1+x-y)^2 - 4x} \approx \frac{8\Delta M^8}{315} , \quad (35)$$

where we have kept only the leading order in ΔM . From these expressions we obtain eq. (24).

References

- [1] ATLAS Collaboration, Phys. Lett. B 716 (2012) 1 [[arXiv:1207.7214](#)].
- [2] CMS Collaboration, Phys. Lett. B 716 (2012) 30 [[arXiv:1207.7235](#)].
- [3] See e.g. A. Strumia, JHEP 1104 (2011) 073 [[arXiv:1101.2195](#)].
- [4] R. Barbieri and D. Pappadopulo, JHEP 0910 (2009) 061 [[arXiv:0906.4546](#)].
- [5] M. Papucci, J. T. Ruderman and A. Weiler, JHEP 1209 (2012) 035 [[arXiv:1110.6926](#)].
- [6] C. Brust, A. Katz, S. Lawrence and R. Sundrum, JHEP 1203 (2012) 103 [[arXiv:1110.6670](#)].
- [7] Z. Han, A. Katz, D. Krohn and M. Reece, JHEP 1208 (2012) 083 [[arXiv:1205.5808](#)].
- [8] J. R. Espinosa, C. Grojean, V. Sanz and M. Trott, [arXiv:1207.7355](#) [hep-ph].
- [9] M. Carena, G. Nardini, M. Quiros and C. E. M. Wagner, JHEP 0810 (2008) 062 [[arXiv:0806.4297](#)].
- [10] <https://twiki.cern.ch/twiki/bin/view/AtlasPublic>
<http://cms.web.cern.ch/org/cms-papers-and-results>
- [11] C. -L. Chou and M. E. Peskin, Phys. Rev. D 61 (2000) 055004 [[hep-ph/9909536](#)].
- [12] G. Hiller, J. S. Kim and H. Sedello, Phys. Rev. D 80 (2009) 115016 [[arXiv:0910.2124](#) [hep-ph]].
- [13] D. S. M. Alves, M. R. Buckley, P. J. Fox, J. D. Lykken and C. -T. Yu, [arXiv:1205.5805](#).
- [14] C. Kilic and B. Tweedie, [arXiv:1211.6106](#).

- [15] The result is obtained updating the fit of P. P. Giardino, K. Kannike, M. Raidal and A. Strumia, [arXiv:1207.1347](#).
- [16] M. Ciuchini, G. Degrassi, P. Gambino and G. F. Giudice, Nucl. Phys. B 534 (1998) 3 [[hep-ph/9806308](#)].
- [17] A. Strumia, Phys. Lett. B 397 (1997) 204 [[hep-ph/9609286](#)].
- [18] E. Gabrielli and G. F. Giudice, Nucl. Phys. B 433 (1995) 3 [Erratum-ibid. B 507 (1997) 549] [[hep-lat/9407029](#)].
- [19] M. Misiak, H. M. Asatrian, K. Bieri, M. Czakon, A. Czarnecki, T. Ewerth, A. Ferroglia and P. Gambino *et al.*, Phys. Rev. Lett. 98 (2007) 022002 [[hep-ph/0609232](#)].
- [20] Heavy Flavor Averaging Group Collaboration, [arXiv:1207.1158](#).
- [21] BABAR Collaboration, [arXiv:1207.5772](#).
- [22] A. J. Bevan *et al.*, PoS HQL 2010 (2011) 019 [<http://utfit.org/UTfit>].
- [23] C. Boehm, A. Djouadi and Y. Mambrini, Phys. Rev. D 61 (2000) 095006 [[hep-ph/9907428](#)].
- [24] A. De Simone, G. F. Giudice and A. Strumia, JHEP 1406 (2014) 081 [[arXiv:1402.6287](#)].
- [25] M. Farina, M. Kadastik, D. Pappadopulo, J. Pata, M. Raidal and A. Strumia, Nucl. Phys. B 853 (2011) 607 [[arXiv:1104.3572](#)]. M. Kadastik, K. Kannike, A. Racioppi and M. Raidal, JHEP 1205 (2012) 061 [[arXiv:1112.3647](#)].
- [26] G. Hiller and Y. Nir, JHEP 0803 (2008) 046 [[arXiv:0802.0916](#)].
- [27] CMS Collaboration, JHEP 1209, 094 (2012) [[arXiv:1206.5663](#)].
- [28] ATLAS Collaboration, [arXiv:1210.4491](#).
- [29] ATLAS Collaboration, Phys. Lett. B 710, 67 (2012) [[arXiv:1109.6572](#)].
- [30] [ATLAS conference note 2012-166](#).
- [31] CMS Collaboration, [arXiv:1210.8115](#).
- [32] C. Rogan, [arXiv:1006.2727](#).
- [33] CMS Collaboration, [arXiv:1212.6961](#).
- [34] T. Sjostrand, S. Mrenna and P. Z. Skands, Comput. Phys. Commun. 178, 852 (2008) [[arXiv:0710.3820](#)].
- [35] M. Cacciari, G. P. Salam and G. Soyez, Eur. Phys. J. C 72, 1896 (2012) [[arXiv:1111.6097](#)].
- [36] M. Cacciari and G. P. Salam, Phys. Lett. B 641, 57 (2006) [[hep-ph/0512210](#)].
- [37] M. Cacciari, G. P. Salam and G. Soyez, JHEP 0804, 063 (2008) [[arXiv:0802.1189](#)].
- [38] The details on how to implement the CMS razor analyses outside the CMS analysis framework are given in <https://twiki.cern.ch/twiki/bin/view/CMSPublic/RazorLikelihoodHowTo>.
- [39] CMS Collaboration, JHEP 1208, 110 (2012) [[arXiv:1205.3933](#)].
- [40] P. J. Fox, R. Harnik, R. Primulando and C. -T. Yu, Phys. Rev. D 86, 015010 (2012) [[arXiv:1203.1662](#)].
- [41] M. Kramer, A. Kulesza, R. van der Leeuw, M. Mangano, S. Padhi, T. Plehn and X. Portell, [arXiv:1206.2892](#).

- [42] Z.-H. Yu, X.J. Bi, Q.-S. Yan, P.-F. Yin, arXiv:[1211.2997](#).
- [43] K. Kriza, A. Kumar, D.E. Morissey, arXiv:[1212.4856](#).
- [44] CMS Collaboration, CMS-PAS-SUS-11-024.